Does low-viscosity fracturing fluid always create complex fractures?

Zhiqiang Chen[1], Derek Elsworth[2], and Moran Wang[1]

[1]Tsinghua University
[2]Pennsylvania State University

November 24, 2022

Abstract

Lower-viscosity fluids are commonly believed to be able to create more complex fractures in hydraulic fracturing, however, the mechanism remains stubbornly unclear. We use a new grain-scale model with accurate coupling of hydrodynamic forces to simulate the propagation of fluid-driven fracturing. The results clarify that fracturing fluid with a lower viscosity does not always create more complex fractures. The heterogeneity in the rock exerts the principal control on systematic evolution of fracture complexity. In homogeneous rock, low viscosity fluids result in low breakdown pressure, but viscosity exerts little influence on fracture complexity. However, in heterogeneous rock, lower viscosity can lead to more complex network of fracturing. A regime map shows the dependence of fracture complexity on the degree of rock heterogeneity where low viscosity fracturing fluid more readily permeates weak defects and creates complex fracture networks.

Does low-viscosity fracturing fluid always create complex fractures?

Zhiqiang Chen[1], Derek Elsworth[2] and Moran Wang[1†]

1. *Department of Engineering Mechanics and CNMM, Tsinghua University, Beijing 100084, China.*
2. *Department of Geosciences, EMS Energy Institute and G3 Center, The Pennsylvania State University, University Park, PA 16802, USA*

Abstract: Lower-viscosity fluids are commonly believed to be able to create more complex fractures in hydraulic fracturing, however, the mechanism remains stubbornly unclear. We use a new grain-scale model with accurate coupling of hydrodynamic forces to simulate the propagation of fluid-driven fracturing. The results clarify that fracturing fluid with a lower viscosity does not always create more complex fractures. The heterogeneity in the rock exerts the principal control on systematic evolution of fracture complexity. In homogeneous rock, low viscosity fluids result in low breakdown pressure, but viscosity exerts little influence on fracture complexity. However, in heterogeneous rock, lower viscosity can lead to more complex network of fracturing. A regime map shows the dependence of fracture complexity on the degree of rock heterogeneity where low viscosity fracturing fluid more readily permeates weak defects and creates complex fracture networks.

Keyword: hydraulic fracturing, fracture complexity, solid-fluid coupling, grain-scale modeling

[†] Corresponding author: Email: mrwang@tsinghua.edu.cn; Tel: +86-10-627-87498

1. Introduction

Hydraulic fracturing is an important stimulation technique in tight or unconventional reservoirs to enable gas or oil production [*Economides and Nolte*, 1989; *Montgomery and Smith*, 2010]. In this process, a significant volume of fluid (fracturing fluid) is injected into the wellbore under high pressure to fracture the rock and drastically increase the permeability-of and production-from the formation [*Economides and Nolte*, 1989]. Hydraulic fracturing is a strongly-coupled fluid-solid process with its efficiency depending on the properties of both the fluid and the rock. The mechanical properties and stress-state of the rock are intrinsic for a specific reservoir, so various fracturing fluids have been used to achieve different fracturing outcomes – principally related to a desired increase in fracture complexity [*Barati and Liang*, 2014; *Wanniarachchi et al.*, 2017]. High viscosity fluids such as cross-linked gels are typically used due to their capacity to effectively transport proppants [*Wanniarachchi et al.*, 2017]. Such fracturing fluids typically result in a single bi-wing planar crack as described by classical theories of hydraulic fracturing [*M K Fisher et al.*, 2002]. The single bi-wing planar fracture is suitable for reservoirs with moderate permeability, which is equivalent to increasing the length or surface area of the wellbore. However, in ultra-low permeability reservoirs, such as gas shales, a simple planar fracture is ineffective – it cannot provide large contact area with the reservoir and reduced diffusive pathway lengths and fails to improve productivity [*M K Fisher et al.*, 2002; *M J Mayerhofer et al.*, 2010]. For example, Barnett Shale was rendered commercially successful by a shift in fracturing fluids in 1998 [*M Fisher et al.*, 2004].

A blend of water with friction reducers (slickwater) was able to generate more complex fracture networks and yield economically viable production of gas [*M Mayerhofer et al.*, 1997]. After that "water fracs" and the concept of "Stimulated Reservoir Volume" (meaning extremely complex fracture network) were widely accepted [*M J Mayerhofer et al.*, 2010; *M J Mayerhofer et al.*, 2006]. The development of hydraulic fracture operations indicates that fracturing fluid has a significant effect on the fracture complexity. This effect is usually qualitatively attributed to the fluid viscosity, but the direct quantitative evidence is still lacking and understanding the in-depth mechanism remains insufficiently clear [*Song et al.*, 2019]. Owing to the difficulty in experimentally observing the fracturing behavior, numerical explorations is needed to reveal what happens in rock during the hydraulic fracturing process.

Generally, there are two kinds of methods in simulating hydro-fracturing, continuum-scale models and grain-scale models. Continuum-scale models such as KGD and PKN representations are routinely applied in the design of hydraulic fracture treatments[*Geertsma and De Klerk*, 1969; *Nordgren*, 1972], where a single planar crack is usually assumed and typically exclude the potential for complex fracturing behavior [*Adachi et al.*, 2007; *Barbati et al.*, 2016; *Detournay*, 2016; *Hubbert and Willis*, 1972]. To consider the fracture network, discrete fracture network (DFN) model is widely used to predict the hydro-fracturing in unconventional reservoirs. *Li and Zhang* (2019) simulated the gases fracturing by DFN, and found CO_2 can induce more complex fracture network than water [*Li and Zhang*, 2019]. However, in DFN models, the fracture information (such as fracture direction, length and amount) should be preset, and the complex fracturing behavior in rock (such as branching and fracture-fracture interaction) is difficultly described. As an alternative, grain-scale models are developed to explore the deeper mechanisms [*Al‐Busaidi et al.*, 2005; *S. A. Galindo-Torres et al.*, 2013; *Shimizu et al.*, 2011], and among them discrete element method (DEM) [*Cundall and Strack*, 1979; *S Galindo-Torres et al.*, 2012] is a promising one. Different from the traditional material such as metal, rock is a "discontinuum" material, comprising grains, pores and pre-existing flaws, so its fracturing behavior is peculiar and complex. DEM directly represents the grain-scale structure of rock by treating each grain as a DEM particle and can hence capture the complex fracturing of rock automatically.

In this work a LBM-DEM coupled model [*Z Chen and Wang*, 2017; *Z Chen et al.*, 2016; *S. A. Galindo-Torres*, 2013; *Min Wang et al.*, 2016] is used to explore why different fluids result in different fracturing behaviors, and in particular focuses on the role of viscosity on evolving fracture complexity. In such models, rock deformation and fracturing behavior is described by DEM. More important, fluid flow is simulated by solving the Navier-Stokes equations directly using the lattice Boltzmann method (LBM), which overcomes the limitation of Darcy's law in continuum-scale models. Darcy's law is based on the creep flow assumption, but during the hydro-fracturing Darcy's law may break down owing to the extremely high fluid pressure. We introduce this grain-scale numerical method in Section 2, which combines the lattice Boltzmann method (LBM), discrete element method (DEM) and the improved IMB method. We then apply this method to explore the evolution of fracture complexity when rock heterogeneity and variable viscosity fluids are used to develop fluid-driven fractures.

2. Grain-scale numerical models for hydro-mechanical coupling

Discrete element methods (DEM) are popular in simulating the mechanical behavior of granular system such as sand, soil, and rock [*Z Chen et al.*, 2018a; *Cundall and Strack*, 1979; *Damjanac and Cundall*, 2016; *S Galindo-Torres et al.*, 2012]. In DEM, the material is discretized as an assembly of discrete bonded particles where the mechanical behavior is obtained by tracking the movement of each particle by integrating Newton's Second Law in time. The external force acting on the DEM particles includes two parts - the collision force and the cohesive force. Current DEM framework is based on the open source software MechSys developed by [*S. A. Galindo-Torres*, 2013], where non-spherical particles can be considered.

In order to consider the effects of cementation, cohesive forces between two adjacent particles are assumed in normal ($\boldsymbol{n}$) and tangential ($\boldsymbol{t}$) directions, which are given by [*S. A. Galindo-Torres et al.*, 2013]

$$\begin{cases} \boldsymbol{F}_n^{cohe} = M_n^{cohe} A \varepsilon_n \boldsymbol{n} \\ \boldsymbol{F}_t^{cohe} = M_t^{cohe} A \varepsilon_t \boldsymbol{t} \end{cases}, \tag{1}$$

where $\boldsymbol{F}_n^{cohe}$ and $\boldsymbol{F}_t^{cohe}$ are cohesive forces, M_n^{cohe} and M_t^{cohe} are the elastic moduli of the virtual cements, ε_n and ε_t are the strains as the two adjacent faces separate and A is the shared interface area. When the strain reaches a threshold value ε_{th},

$$\frac{|\varepsilon_n| + |\varepsilon_t|}{\varepsilon_{th}} > 1, \tag{2}$$

the cohesive forces vanish, and a crack is induced along the common interface shared by the two adjacent particles.

The second external force is the collision force and results when two particles collide. In the current simulation, a spring model is used

$$\begin{cases} \boldsymbol{F}_n^{cont} = K_n \Delta l_n \boldsymbol{n} \\ \boldsymbol{F}_t^{cont} = K_t \Delta l_t \boldsymbol{t} \end{cases}, \tag{3}$$

where $\boldsymbol{F}_n^{cont}$ and $\boldsymbol{F}_t^{cont}$ are collision forces, K_n and K_t are spring stiffnesses, Δl_n and Δl_t are the length of interpenetration in the normal and tangential directions, respectively. The efficiency of current DEM scheme in simulating mechanical behavior of the rock material can be found in our previous work [*Z Chen et al.*, 2018a].

The lattice Boltzmann method (LBM) is a numerical method for fluid flow and makes the Navier-Stokes equations solved [*S Chen and Doolen*, 1998]. However, different from the traditional computational fluid dynamics (CFD) methods, the basic variable in LBM is the density distribution function rather than more usual macroscopic parameters (such as pressure and velocity). Here, a three dimensional 15-speed model (D3Q15) is applied[*Moran Wang and Chen*, 2007; *Zhang and Wang*, 2017], where the evolution equation is written as

$$f_i\left(\boldsymbol{x}+\boldsymbol{e}_i\delta_t, t+\delta_t\right) = f_i\left(\boldsymbol{x},t\right) - \frac{1}{\tau}\left(f_i\left(\boldsymbol{x},t\right) - f_i^{eq}\left(\boldsymbol{x},t\right)\right),\ i = 0-14 \quad, \tag{4}$$

where f_i is the density distribution in the *i-th* the discrete velocity direction $\boldsymbol{e}_i$, f_i^{eq} is the corresponding equilibrium distribution, and δ_t is the time step. Parameter τ is the dimensionless relaxation time and reflects the fluid kinematic viscosity

$$\nu = \frac{\left(\tau - 1/2\right)\delta_x^2}{3\delta_t}, \tag{5}$$

where δ_x is the grid size. In the D3Q15 model, the discrete velocity $\boldsymbol{e}$ has 15 directions

$$e = c\begin{bmatrix} 0 & 1 & 0 & -1 & 0 & 0 & 0 & 1 & 1 & 1 & 1 & -1 & -1 & -1 & -1 \\ 0 & 0 & 0 & 0 & 0 & -1 & 1 & -1 & -1 & 1 & 1 & -1 & -1 & 1 & 1 \\ 0 & 0 & 1 & 0 & -1 & 0 & 0 & 1 & -1 & -1 & 1 & 1 & -1 & -1 & 1 \end{bmatrix}, \tag{6}$$

where $c = \delta_x / \delta_t$. The equilibrium distribution in the *i-th* direction is written as

$$f_i^{eq}(\rho, \boldsymbol{u}) = \rho\omega_i \left[1 + \frac{3\boldsymbol{e}_i \cdot \boldsymbol{u}}{c^2} + \frac{9(\boldsymbol{e}_i \cdot \boldsymbol{u})^2}{2c^4} - \frac{3\boldsymbol{u} \cdot \boldsymbol{u}}{2c^2}\right], \tag{7}$$

where the weighting factors are

$$\omega_i = \begin{cases} 2/9, & i = 0 \\ 1/9, & i = 1-6 \\ 1/72, & i = 7-14 \end{cases} . \tag{8}$$

The fluid density and velocity are calculated as

$$\rho = \sum_i f_i \quad , \tag{9}$$

$$\rho\boldsymbol{u} = \sum_i f_i \boldsymbol{e}_i , \tag{10}$$

and the pressure p is given by

$$p = \frac{1}{3}\rho c^2 . \tag{11}$$

In the previous LBM-DEM coupled models, an immersed moving boundary (IMB) is typically applied to facilitate fluid solid interaction [*S. A. Galindo-Torres*, 2013; *Noble and Torczynski*, 1998; *Min Wang et al.*, 2016] – however, the hydrodynamic force provided by this method is insufficiently accurate to represent stresses at fluid-filled crack-tips. To overcome this limitation, an improved IMB method proposed in our previous work is applied in this work.

In this improved IMB method, the evolution equation in LBM is modified as

$$f_i(\boldsymbol{x} + \boldsymbol{e}_i\delta_t, t + \delta_t) = f_i(\boldsymbol{x}, t) - (1 - B)\frac{1}{\tau}\left(f_i(\boldsymbol{x}, t) - f_i^{eq}(\boldsymbol{x}, t)\right) + B\Omega_i^s . \tag{12}$$

The parameter Ω is the fluid-solid interaction term, which is calculated by the bounce-back for the non-equilibrium part of the density distribution

$$\Omega_i^s = \left[f_{-i}(\boldsymbol{x}, t) - f_{-i}^{eq}(\rho, \boldsymbol{v}_p)\right] - \left[f_i(\boldsymbol{x}, t) - f_i^{eq}(\rho, \boldsymbol{v}_p)\right] \quad , \tag{13}$$

where $\boldsymbol{v}_p$ is the DEM particle velocity at position $\boldsymbol{x}$, weighting factor B is a function of the dimensionless relaxation time (τ) and solid volume fraction of the LBM cell at position $\boldsymbol{x}$ (γ) and is given as

$$B = \frac{\gamma(\tau - 0.5)}{(1-\gamma) + (\tau - 0.5)} . \tag{14}$$

The hydrodynamic force $\boldsymbol{F}$ is calculated by the change in momentum of the fluid covered by the DEM particles, which is given by

$$\boldsymbol{F} = \rho_f V \frac{\boldsymbol{u}_s(t) - \boldsymbol{u}_s(t-\delta_t)}{\delta_t} - \sum_n \sum_i \frac{\delta_x^3 B_n}{\delta_t} \Omega_i^s \boldsymbol{e}_i \quad , \tag{15}$$

$$\boldsymbol{T} = I_f \frac{\boldsymbol{\varpi}_s(t) - \boldsymbol{\varpi}_s(t-\delta_t)}{\delta_t} - \sum_n \left(\sum_i \frac{\delta_x^3 B_n}{\delta_t} \Omega_i^s \boldsymbol{e}_i (\boldsymbol{x}_n - \boldsymbol{x}_{cm}) \right) \quad . \tag{16}$$

Compared with the original IMB method, the internal fluid correction (the first term on the right-hand-side of Eqs. 15 and 16) is added to ensure the accuracy of the hydrodynamic force calculation. Parameter V is the volume of the solid particle, $\boldsymbol{u}_s$ and $\boldsymbol{\varpi}_s$ are the linear and angular velocities of the DEM particle, respectively, I_f is the moment of inertia for the internal fluid covered by the DEM particle, $\boldsymbol{x}_n$ is the fluid cell position, and $\boldsymbol{x}_{cm}$ is the mass center of the DEM particle. The validations of this revised LBM-DEM model are given in the Appendix.

3. Results and discussion

The physical model in the current simulation is shown in Figure 1, where the rock matrix is discretized as an assembly of triangular particles bonded with each other (see Figure 1(a)). Fluid is injected into a hole on the left side of the domain with an initial crack introduced near this hole. The sizes of triangular particles in Figure 1(a) are reduced by a small distance to provide flow channels (white part in Figure 1(b)) within the assemblage. Fluid flows only within these channels (simulated by LBM) with the hydrodynamic force imposed on the interior triangular particles calculated by the improved IMB method. These ensemble fluid forces results in the propagation of the discrete hydraulic fracture. In order to capture the effects of the newly formed fracture on flow conductivity a fracture-dependent flow conductivity is applied. When the bond is intact, a high virtual solid volume (γ in Eq. 14) is introduced in the flow channel, corresponding to a low conductivity. When the bond is broken, γ in the corresponding flow channel is set to zero, resulting in high permeability for the newly formed fracture [*S Wang et al.*, 2011]. The purpose of this work is to invest the fluid viscosity effect on the fracture complexity, so to avoid the influence from the confining stresses the samples are unconfined in current model. More details of this LBM-DEM scheme for hydraulic fracture propagation can be found in our previous work [*Z Chen and Wang*, 2017; *Z Chen et al.*, 2018b].

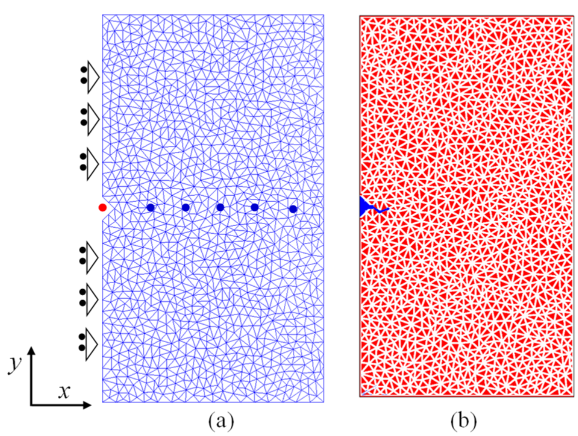

Figure 1. Schematic for LBM-DEM simulation of hydraulic fracturing. (a) Discretization of the rock matrix by triangular particles, where a borehole is set on the left edge to allow fluid injection. (b) The sizes of triangular particles in (a) are reduced by a small distance to provide

flow channels (white) in the rock, where an initial crack (blue) is introduced to guide the subsequent propagation of the hydraulic fracture.

During the simulation, the left edge of the computational domain is set as a symmetric boundary, with the DEM particles to the left fixed in the *x*-direction but free to displace in the *y*-direction. The rock sample is unconfined on other three edges. In order to explore why different fluids potentially generate different fracturing behaviors, various viscosity fluids are injected. Parameters represented in the DEM and LBM models are listed in Table 1.

Table 1. Parameters in DEM and LBM models.

Parameters	**Value**
Normal stiffness, K_n	$1\times10^8\ N/m$
Tangential stiffness, K_t	$1\times10^8\ N/m$
Particle friction coefficient, μ_{fric}	0.4
Normal elastic modulus, M_n^{cohe}	$2.0\times10^9\ Pa$
Tangential elastic modulus, M_t^{cohe}	$4.17\times10^9\ Pa$
Rock matrix bonding strength, ε_{th}	0.01
Fluid density, ρ	$1\times10^3\ kg/m^3$
Lattice size in LBM, δ_x	$1.0\times10^{-4}\ m$
Time step in LBM, δ_t	$2.0\times10^{-7}\ s$

Figure 2 shows the resulting hydraulic fracture driven by different viscosity fluids, where (a), (b) and (c) are fracture geometries for kinematic viscosities of ν= $2\times10^{-3}\ m^2/s$, $1\times10^{-3}\ m^2/s$ and $5\times10^{-4}\ m^2/s$, respectively. Figure 2(d) is the pressure evolution in the borehole (red point in Figure 1(a)) during the progress of the hydraulic fracturing, and

Figure 2(e) is the pressure distribution when the fracture is initially induced, as measured along the central part of the computational domain (1 red point and 5 blue points in Figure 1(a)).

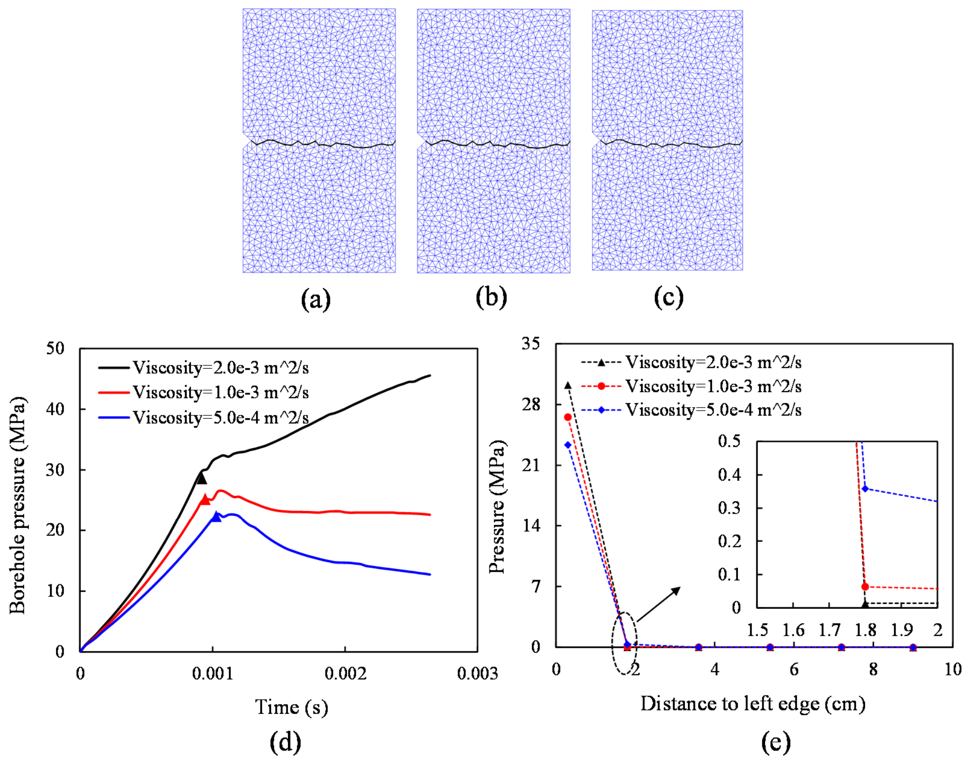

Figure 2. Hydraulic fracture evolution for fluids with contrasting viscosities. Figures (a), (b) and (c) are fracture geometries for kinematic viscosities of $\nu=2\times10^{-3}$ m^2/s, 1×10^{-3} m^2/s and 5×10^{-4} m^2/s, respectively. (d) Pressure evolution in the borehole (red point in Figure 1(a)) during the hydraulic fracturing process. (e) Pressure distribution when the fracture is initially induced.

The evolution of pressure in the borehole is an important indicator of hydraulic fracture propagation. The first pressure drop represents the initiation of the fracture – referenced as the breakdown pressure. Figure 2(d) shows that the pressure increases most rapidly for a higher viscosity and slowest for low viscosity with the breakdown pressure also reducing with a reduction in viscosity. Similar results have also been observed in other experimental and numerical studies [*Chitrala et al.*, 2012; *Gan et al.*, 2015; *J Wang et al.*, 2018]. In order to explain this phenomenon, the pressure distribution along the rock sample is plotted when the fracture is initially induced (Figure 2(e)). The leftmost points in Figure 2(e) are the breakdown pressure for different viscosity fluids. It can be seen that for the low viscosity cases, the breakdown pressure is low although the pore pressure directly adjacent to the hole is high. High pore pressure reduces the effective stress and promotes weakening of the borehole wall. The high pore pressure in the rock matrix for the low viscosity fluid can be attributed to two reasons. First, fluid with low viscosity more easily penetrates into the rock matrix owing to the low flow resistance. Secondly, the pressure buildup for low viscosity case is slow (Figure 2(d)), so fluid has more time to increase the pore pressure adjacent to the borehole wall.

However, these current simulations seem to suggest that viscosity has little effect on fracture geometry. The hydraulic fractures induced by the different fluids are near identical (see Figure 2(a)-(c)), and a thorough-going simple fracture is generated in all samples. However, previous experimental results show that the fluid viscosity is an important parameter affecting the fracture geometry [*Bennour et al.*, 2015]. When high viscosity fluid is used, such as oil, a simple fracture is formed. However, when the fluid viscosity is low, a complex fracture geometry can be induced. Thus, further exploration is needed to deal with this inconsistency.

In the prior simulations, the rock sample is homogeneous - with bond strengths uniformly distributed. However, strength heterogeneity is an important feature of rock owing to the different mineral components. This strength heterogeneity may be quantitatively represented as a Weibull distribution [*McClintock and Zaverl*, 1979]. Thus, the impact of strength heterogeneity may be considered, by setting the bonding strength threshold (ε_{th}) as a random field following the Weibull distribution

$$f\left(\varepsilon_{th}\right)=\frac{m}{\varepsilon_{th}^{0}}\left(\frac{\varepsilon_{th}}{\varepsilon_{th}^{0}}\right)^{m-1}\exp\left(-\left(\frac{\varepsilon_{th}}{\varepsilon_{th}^{0}}\right)^{m}\right), \tag{17}$$

where ε_{th}^{0} is the average bond strength threshold, and m>0 is the shape parameter describing the degree of dispersion of ε_{th} . In current work more than 3000 DEM particles are used, which is considered sufficiently to represent the Weibull distribution [*Rossi and Richer*, 1987]. In order to quantify the degree of heterogeneity, an index (h) between 0 and 1 is proposed, representing the normalized standard deviation of the Weibull distribution as

$$h=\frac{\sigma_{std}}{E_{mean}}=\frac{\Gamma\left(1+1/m\right)}{\sqrt{\Gamma\left(1+2/m\right)-\left(\Gamma\left(1+1/m\right)\right)^{2}}}, \tag{18}$$

where Γ is the gamma function, σ_{std} is the standard deviation, and E_{mean} is the mean of the distribution. When m=1, h=1 and this corresponds to a highly heterogeneous system. Conversely, h=0, represents a totally homogeneous sample.

Figure 3 shows the evolution of the hydraulic fracture in a highly heterogeneous rock sample (h=0.52), where (a) is the fracture geometry induced by fluids with different viscosities. The fracture geometry induced by a low viscosity (9×10^{-5} m^2/s) fluid is more complex than that induced by a high viscosity (2×10^{-3} m^2/s) fluid.

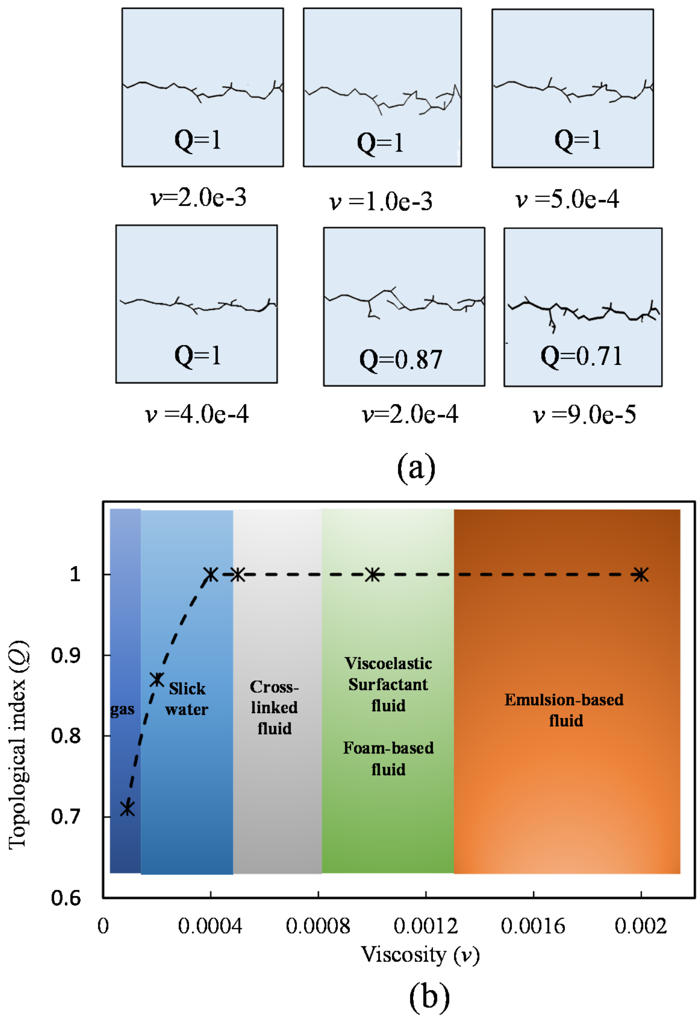

Figure 3. Evolution of a hydraulic fracture in heterogeneous samples. (a) Fracture geometry induced by fluid with viscosity of v=2×10^{-3} m^2/s, 1×10^{-3} m^2/s, 5×10^{-4} m^2/s, 4×10^{-4} m^2/s, 2×10^{-4} m^2/s and 9×10^{-5} m^2/s respectively. (b) Modified topological index representing the various cases - quantitatively indicates that lower viscosity fluids result in more complex fracture networks in heterogeneous rock.

In order to provide a quantitative comparison of fracture complexity induced by different fluids, a modified topological index (Q) is calculated for each case. The parameter Q is an index [*Z Chen and Wang*, 2017] to quantify the complexity of the resulting fracture geometry $0<Q<1$with a lower Q corresponding to a more complex fracture geometry. Figure 3(b) shows that for low viscosity fluids the topological index Q is smaller, which quantitatively demonstrates that in heterogeneous rock low viscosity is conducive to the formation of complex fracture network, similar to experimental observations [*Bennour et al.*, 2015]. Thus, fracturing fluid effects on fracture complexity depends on the rock properties. In homogeneous rock, fluid viscosity has little effects on fracture complexity, but in heterogeneous rock, lower viscosity may result in more complex fracture networks. In order to explain this rock-dependent effect, the evolving pressure distribution in the rock sample is plotted in Figure 4.

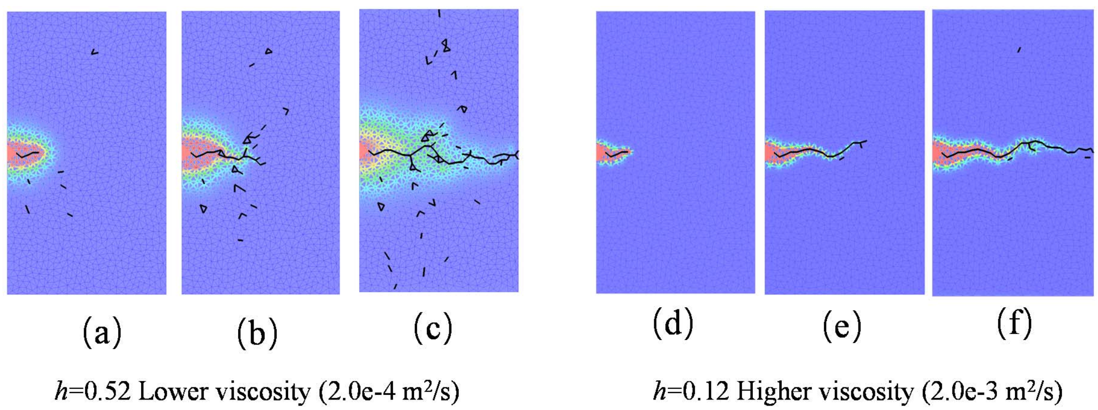

Figure 4. Pressure distribution in rock samples. (a), (b), (c) Evolving pressure distribution with time in highly heterogeneous rock (h=0.52) with low viscosity fluid (2×10^{-4} m^2/s), and (d), (e) and (f) are the evolving pressure distribution in homogeneous rock (h=0.12) with high viscosity fluid (2×10^{-3} m^2/s).

Low viscosity fluid readily penetrates into the rock matrix and elevates pore pressure around the main fracture (see Figure 4(a), (b) and (c)). In heterogeneous rock (h=0.52), the weak bonds close to the main fracture are readily broken by the high induced pore pressure (low viscosity injection), allowing the nucleation of cracks. These nucleated cracks connect to the main fracture and form a connective branch (see Figure 4(c)), generating the nucleus of a nascent complex fracture network. However, in homogeneous rock, bond strengths are uniformly distributed with no weak bonds existing to form such crack nucleation and branches. Thus, although low viscosity fluid can result in high pore pressures in homogeneous samples, the generation of complex fracture networks is impeded.

In summary, it is the degree of heterogeneity of the rock that controls the impact of fluid viscosity on the ensuing fracture complexity. In homogeneous samples, fluid viscosity does not affect the fracture complexity, just as the prediction in continuum-based models. However, in heterogeneous samples, a lower viscosity fluid results in the development of more complex fracture networks - consistent with experimental observations in real rock.

To probe the evolution of fracture complexity under different conditions, the impacts of heterogeneity and viscosity are explored by systematically varying both heterogeneity (h= 0.12, 0.23 and 0.52) and viscosity (ν=2×10^{-3} m^2/s, 5×10^{-4} m^2/s，2×10^{-4} m^2/s and 9×10^{-5} m^2/s) to explore the parameter space. Figure 5 is a regime map showing fracture complexity (Q) as a function of that (h, ν) parameter space. The evolution of complex fractures fall at the intersection of the higher heterogeneity and lower viscosity regions. Conversely, simple fractures evolve for the lower heterogeneity and higher viscosity cases. For each heterogeneity index h, a critical viscosity exits, below which the transition from a simple crack to a complex fracture network occurs. This critical viscosity increases with an increase of the degree of heterogeneity of the rock. Thus, if a complex hydraulic fracture network is desired then two key points should be noted. First, a necessary condition exists such that the degree of heterogeneity of the rock must be high - such as in reservoirs rich with natural fractures. And second, networks of complex fractures are maximally promoted where a fracturing fluid with a low viscosity is utilized, such as in “gas fracturing”.

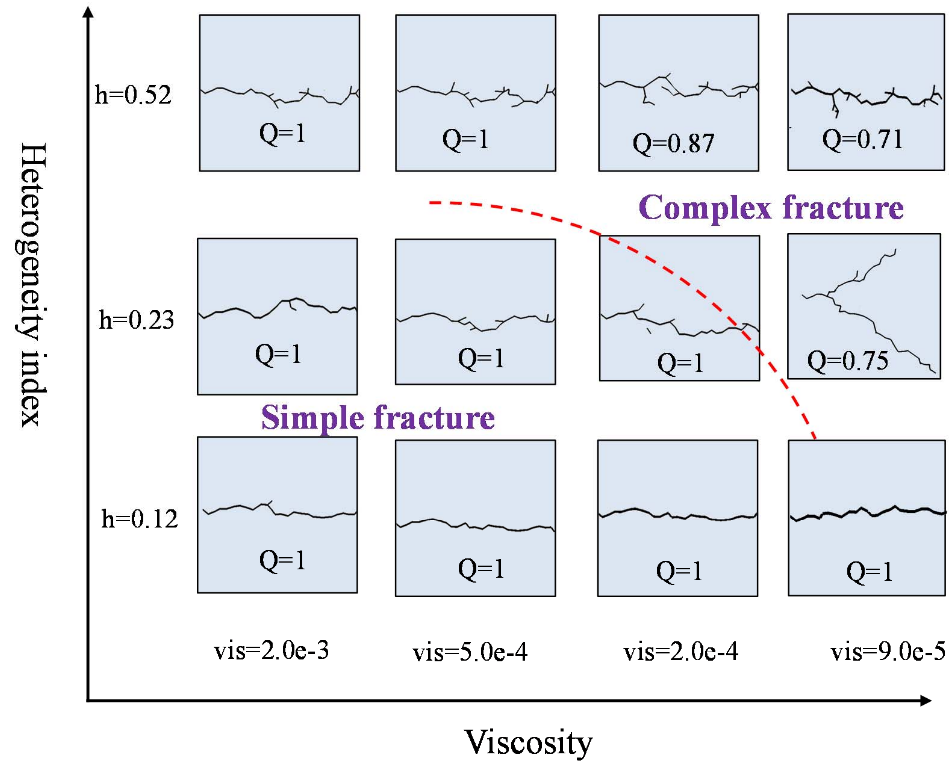

Figure 5. Regime map showing the distribution of fracture complexity (Q) in a (h, γ) diagram. Complex fractures fall at the intersection of regions of high heterogeneity and low viscosity. Simple fractures are favored for reduced heterogeneity and elevated viscosity.

4. Conclusions

In this study, a grain-scale LBM-DEM coupled model is applied to simulate the evolution of hydraulic fractures with a focus on why different fluids result in different fracturing behaviors. To improve the accuracy of the hydrodynamic force calculation, an improved IMB method is applied. The fluid viscosity impacts fracturing behavior only through the level of heterogeneity of the rock. In homogeneous rock, fluid viscosity only impacts the breakdown pressure (low viscosity corresponding to low breakdown pressure) to initiate a fracture, but exerts little influence on the ensuing fracture complexity (a similar simple fracture is induced no matter what kind of fluid is used). Conversely, in heterogeneous rock, fluid viscosity significantly impacts fracture complexity, with lower viscosity fluids resulting in more complex fracture networks. This is contributed by the presence of weak bonds (representing natural fractures or weak defects) present near the main fracture, which are easily broken by the invading high pore pressure and form discrete fracture branches. The low viscosity fluid promotes the ready buildup of pore pressures in the rock matrix enabling a complex fracture network to be more readily induced. A regime map showing the fracture complexity (Q) distribution in an (h, v) diagram is presented, which indicates that complex fracturing is promoted in the intersection of the low viscosity and high heterogeneity regions. Thus, rock properties (heterogeneity) and fluid properties (viscosity) are two key factors governing the evolution of fracture complexity during hydraulic fracture treatments. Thus, in unconventional reservoirs, the development of complex fracture networks from heterogeneous reservoirs probed by lower viscosity fluids may increase both the rate and absolute recovery of the hydrocarbon resource.

Acknowledgements: This work is financially supported by the NSF grant of China (No. 11761131012, U1837602). According to AGU’s Data Policy, we declare no data used in this work. There is no conflict of interest in this work.

Appendix

In this part, current hydro-mechanical coupled framework is validated, including lattice Boltzmann method in simulating the fluid flow, discrete element method in describing the fracturing behavior of rock and the improved immersed boundary method in calculating the hydrodynamic force.

A1. Validation of lattice Boltzmann method

To test the current LBM model, fluid flow in a two dimensional channel is simulated. The physical model is presented in Figure A1 (a), where L and H is the length and width of the channel respectively. A pressure difference ΔP is applied in the Y direction. In the equilibrium state, fluid velocity distribution in the X direction can be obtained analytically

$$u = \frac{1}{2\mu}\frac{\Delta P}{L}\left[\frac{H^2}{4} - \left(x - \frac{H}{2}\right)^2\right]. \tag{A1}$$

Figure A1 (b) shows the comparison between the analytical solution and numerical results, and good agreement is obtained.

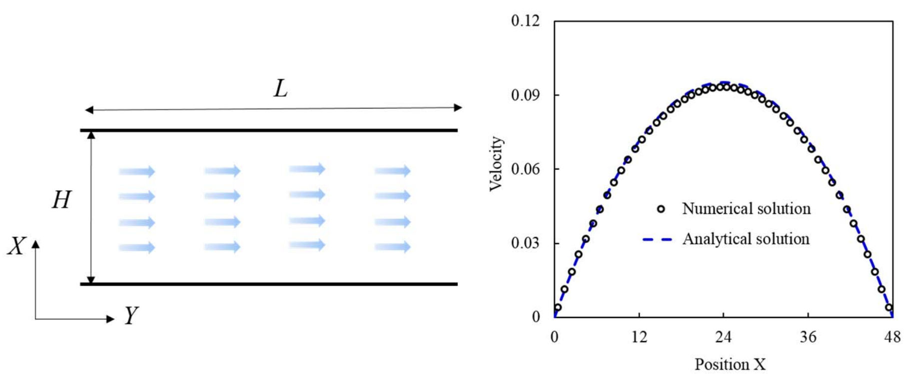

(a) (b)

Figure A1. (a) Physical model of LBM simulation of fluid flow along 2 dimensionless channel, where L and H is the length and width of the channel respectively. A pressure difference is applied in Y direction to drive the fluid motion. (b) Comparison between analytical solution and numerical result, which shows that good agreement is obtained.

A2. Validation of discrete element method

To validate the current DEM model in capturing the fracturing behavior of rock, Brazilian test is simulated, where a disc sample, discretized into a collection of triangle particles (see Figure A2 (a)), is compressed along the direction parallel to its diameter.

Figure A2 (b) shows the disc is split into two halves along the diameter, which is the typical feature of Brazilian test. The stress-strain relation during the compression process is also recorded, and the slope and peak value in Figure A2 (c) corresponds to the elasticity modulus and tensile strength, respectively.

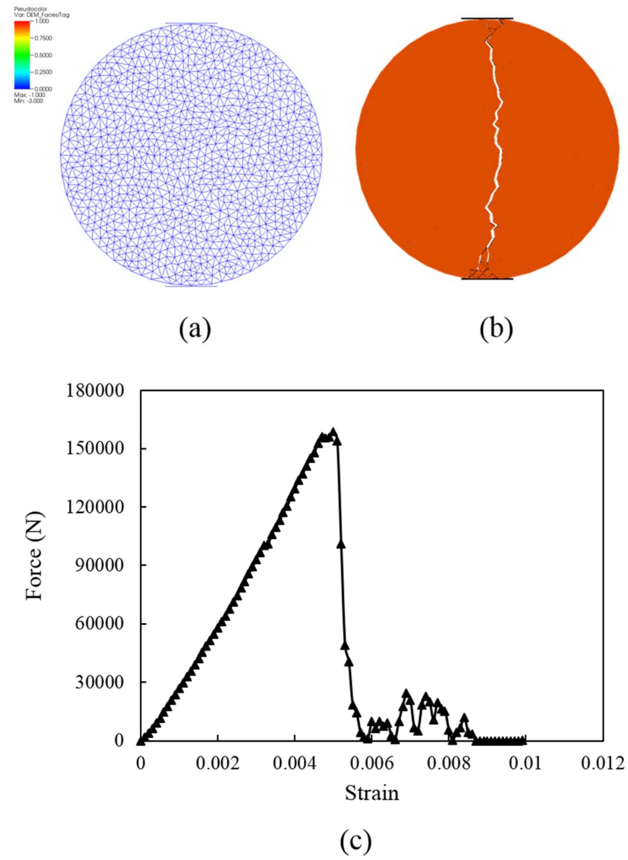

Figure A2. (a) Physical model of Brazilian test simulation, where the disc sample is discretized into a collection of triangle particles, which is compressed along the diameter. (b) The resulting fracture after the Brazilian test, which shows that current DEM model successfully capture the main feature of the fracturing behavior of rock. (c) Stress-strain relation during the compression process, where the slope and peak value corresponds to the elasticity modulus and tensile strength, respectively.

A3. Validation of improved immersed moving boundary

In hydro-mechanical coupled model, a key point is the accurate calculation of the hydrodynamic force imposed on the solid surface. In this part, a single elliptical particle sedimentation in the Newtonian fluid is simulated to validate current improved IMB method. The physical model is presented in Figure A3 (a), where *a* and *b* is the length of the semiminor and semimajor axis of the elliptical particle, respectively. The width of channel is 0.4 *cm*, and the length is long enough (12 *cm*) to avoid the boundary influence. The particle is initially placed at the position (1.2 *cm*, 0.2 *cm*) with $\alpha=3\pi/4$. A constant gravity force in the x direction is applied on the particle, which determines the terminal particle Reynolds number ($Re=Vb/\nu$). In this case, the terminal particle Reynolds number is equal to 6.6. The particle trajectory obtained with different methods is shown in Figure A3 (b). Current model agrees well with the FEM results in Ref. [*Xia et al.*, 2009], but the deviation exists in previous one. Thus, current improved IMB model can give the accurate calculation of hydrodynamic force applied on the solid surface.

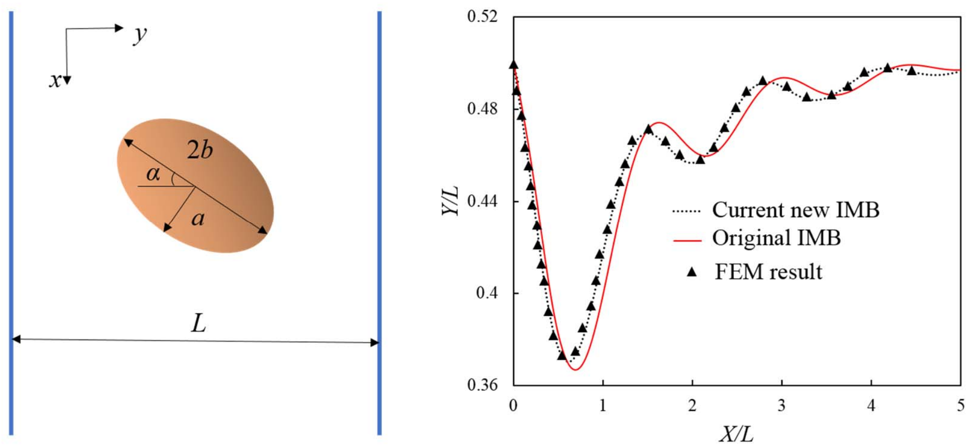

Figure A3. (a) Physical model of an elliptical particle sedimentation in the Newtonian fluid, where a and b is the length of the semiminor and semimajor axis of the elliptical particle, respectively. A constant gravity force is applied on the particle to drive its motion in the x direction. (b) The particle trajectory obtained with different methods, which shows that current model agrees well with the FEM results in Ref. [*Xia et al.*, 2009], but the deviation exists in previous one.

Reference

Adachi, J., E. Siebrits, A. Peirce, and J. Desroches (2007), Computer simulation of hydraulic fractures, *International Journal of Rock Mechanics and Mining Sciences*, *44*(5), 739-757.

Al‐Busaidi, A., J. Hazzard, and R. Young (2005), Distinct element modeling of hydraulically fractured Lac du Bonnet granite, *Journal of geophysical research: solid earth*, *110*(B6).

Barati, R., and J. T. Liang (2014), A review of fracturing fluid systems used for hydraulic fracturing of oil and gas wells, *Journal of Applied Polymer Science*, *131*(16).

Barbati, A. C., J. Desroches, A. Robisson, and G. H. McKinley (2016), Complex fluids and hydraulic fracturing, *Annual review of chemical and biomolecular engineering*, *7*, 415-453.

Bennour, Z., T. Ishida, Y. Nagaya, Y. Chen, Y. Nara, Q. Chen, K. Sekine, and Y. Nagano (2015), Crack extension in hydraulic fracturing of shale cores using viscous oil, water, and liquid carbon dioxide, *Rock Mechanics and Rock Engineering*, *48*(4), 1463-1473.

Chen, S., and G. D. Doolen (1998), Lattice Boltzmann method for fluid flows, *Annual Review of Fluid Mechanics*, *30*, 329-364.

Chen, Z., X. Jin, and M. Wang (2018a), A new thermo-mechanical coupled DEM model with non-spherical grains for thermally induced damage of rocks, *Journal of the Mechanics and Physics of Solids*, *116*, 54-69.

Chen, Z., and M. Wang (2017), Pore-scale modeling of hydromechanical coupled mechanics in hydrofracturing process, *Journal of Geophysical Research-Solid Earth*, *122*(5), 3410-3429, doi:10.1002/2017jb013989.

Chen, Z., C. Y. Xie, Y. Chen, and M. Wang (2016), Bonding Strength Effects in Hydro-Mechanical Coupling Transport in Granular Porous Media by Pore-Scale Modeling, *Computation*, *4*(1), 18, doi:10.3390/computation4010015.

Chen, Z., Z. Yang, and M. Wang (2018b), Hydro-mechanical coupled mechanisms of hydraulic fracture propagation in rocks with cemented natural fractures, *Journal of Petroleum Science and Engineering*, *163*, 421-434, doi:10.1016/j.petrol.2017.12.092.

Chitrala, Y., C. Sondergeld, and C. Rai (2012), Acoustic emission studies of hydraulic fracture evolution using different fluid viscosities, paper presented at 46th US Rock Mechanics/Geomechanics Symposium, American Rock Mechanics Association.

Cundall, P. A., and O. D. Strack (1979), A discrete numerical model for granular assemblies, *geotechnique*, *29*(1), 47-65.

Damjanac, B., and P. Cundall (2016), Application of distinct element methods to simulation of hydraulic fracturing in naturally fractured reservoirs, *Computers and Geotechnics*, *71*, 283-294.

Detournay, E. (2016), Mechanics of hydraulic fractures, *Annual Review of Fluid Mechanics*, *48*, 311-339.

Economides, M. J., and K. G. Nolte (1989), *Reservoir stimulation*, Prentice Hall Englewood Cliffs, NJ.

Fisher, M., J. Heinze, C. Harris, B. Davidson, C. Wright, and K. Dunn (2004), Optimizing horizontal completion techniques in the Barnett shale using microseismic fracture mapping, paper presented at SPE Annual Technical Conference and Exhibition, Society of Petroleum Engineers.

Fisher, M. K., C. A. Wright, B. M. Davidson, A. Goodwin, E. Fielder, W. Buckler, and N. Steinsberger (2002), Integrating fracture mapping technologies to optimize stimulations in the Barnett Shale, *SPE annual technical conference and exhibition*.

Galindo-Torres, S., D. Pedroso, D. Williams, and L. Li (2012), Breaking processes in three-dimensional bonded granular materials with general shapes, *Computer Physics Communications*, *183*(2), 266-277.

Galindo-Torres, S. A. (2013), A coupled Discrete Element Lattice Boltzmann Method for the simulation of fluid-solid interaction with particles of general shapes, *Computer Methods in Applied Mechanics and Engineering*, *265*, 107-119, doi:10.1016/j.cma.2013.06.004.

Galindo-Torres, S. A., D. M. Pedroso, D. J. Williams, and H. B. Muhlhaus (2013), Strength of non-spherical particles with anisotropic geometries under triaxial and shearing loading configurations, *Granular Matter*, *15*(5), 531-542, doi:10.1007/s10035-013-0428-6.

Gan, Q., D. Elsworth, J. Alpern, C. Marone, and P. Connolly (2015), Breakdown pressures due to infiltration and exclusion in finite length boreholes, *Journal of Petroleum Science and Engineering*, *127*, 329-337.

Geertsma, J., and F. De Klerk (1969), A rapid method of predicting width and extent of hydraulically induced fractures, *Journal of Petroleum Technology*, *21*(12), 1,571-571,581.

Hubbert, M. K., and D. G. Willis (1972), Mechanics of hydraulic fracturing.

Li, S., and D. Zhang (2019), How effective is carbon dioxide as an alternative fracturing fluid?, *SPE Journal*, *24*(02), 857-876.

Mayerhofer, M., M. Richardson, R. Walker Jr, D. Meehan, M. Oehler, and R. Browning Jr (1997), Proppants? We don't need no proppants, paper presented at SPE Annual Technical Conference and Exhibition, Society of Petroleum Engineers.

Mayerhofer, M. J., E. Lolon, N. R. Warpinski, C. L. Cipolla, D. W. Walser, and C. M. Rightmire (2010), What is stimulated reservoir volume?, *SPE Production & Operations*, *25*(01), 89-98.

Mayerhofer, M. J., E. P. Lolon, J. E. Youngblood, and J. R. Heinze (2006), Integration of microseismic-fracture-mapping results with numerical fracture network production modeling in the Barnett Shale, paper presented at SPE annual technical conference and exhibition, Society of Petroleum Engineers.

McClintock, F., and F. Zaverl (1979), An analysis of the mechanics and statistics of brittle crack initiation, *International Journal of Fracture*, *15*(2), 107-118.

Montgomery, C. T., and M. B. Smith (2010), Hydraulic fracturing: history of an enduring technology, *Journal of Petroleum Technology*, *62*(12), 26-40.

Noble, D. R., and J. R. Torczynski (1998), A lattice-Boltzmann method for partially saturated computational cells, *International Journal of Modern Physics C*, *9*(8), 1189-1201, doi:10.1142/s0129183198001084.

Nordgren, R. (1972), Propagation of a vertical hydraulic fracture, *Society of Petroleum Engineers Journal*, *12*(04), 306-314.

Rossi, P., and S. Richer (1987), Numerical modelling of concrete cracking based on a stochastic approach, *Materials and Structures*, *20*(5), 334-337.

Shimizu, H., S. Murata, and T. Ishida (2011), The distinct element analysis for hydraulic fracturing in hard rock considering fluid viscosity and particle size distribution, *International Journal of Rock Mechanics and Mining Sciences*, *48*(5), 712-727.

Song, X., Y. Guo, J. Zhang, N. Sun, G. Shen, X. Chang, W. Yu, Z. Tang, W. Chen, and W. Wei (2019), Fracturing with Carbon Dioxide: From Microscopic Mechanism to Reservoir Application, *Joule*.

Wang, J., D. Elsworth, Y. Wu, J. Liu, W. Zhu, and Y. Liu (2018), The influence of fracturing fluids on fracturing processes: a comparison between water, oil and SC-CO 2, *Rock Mechanics and Rock Engineering*, *51*(1), 299-313.

Wang, M., and S. Chen (2007), Electroosmosis in homogeneously charged micro- and nanoscale random porous media, *Journal of Colloid and Interface Science*, *314*(1), 264-273, doi:10.1016/j.jcis.2007.05.043.

Wang, M., Y. Feng, and C. Wang (2016), Coupled bonded particle and lattice Boltzmann method for

modelling fluid–solid interaction, *International Journal for Numerical and Analytical Methods in Geomechanics*, *40*(10), 1383-1401.
Wang, S., D. Elsworth, and J. Liu (2011), Permeability evolution in fractured coal: the roles of fracture geometry and water-content, *International Journal of Coal Geology*, *87*(1), 13-25.
Wanniarachchi, W., P. Ranjith, and M. Perera (2017), Shale gas fracturing using foam-based fracturing fluid: a review, *Environmental Earth Sciences*, *76*(2), 91.
Xia, Z., K. W. Connington, S. Rapaka, P. Yue, J. J. Feng, and S. Chen (2009), Flow patterns in the sedimentation of an elliptical particle, *Journal of Fluid Mechanics*, *625*, 249-272.
Zhang, L., and M. Wang (2017), Electro-osmosis in inhomogeneously charged microporous media by pore-scale modeling, *Journal of Colloid and Interface Science*, *486*, 219-231, doi:10.1016/j.jcis.2016.09.057.